

Strain-enhanced optical gain of hexagonal Ge nanowire

Xue-Li Zhao(赵雪丽), Shan Guan(管闪), Zhigang Song(宋志刚), and Jun-Wei Luo(骆军委)
Citation: Chin. Phys. B, 2026, 35 (**6**): 067303. DOI: 10.1088/1674-1056/ae53b7
http://cpb.iphy.ac.cn; http://iopscience.iop.org/cpb

What follows is a list of articles you may be interested in

Ultra-high anisotropy and electronic property of two-dimensional $PbSnS_2$ with a black phosphorus structure

Xinlong Wang(王鑫龙), Shihao Wang(王诗皓), Yandi Jiang(姜彦迪), Qing Min(闵清), Haiming Huang(黄海铭), Chengrui Wu(吴承瑞), and Juntao Yang(杨俊涛)
Chin. Phys. B, 2026, 35 (**5**): 057304. DOI: 10.1088/1674-1056/ae1568

Exciton insulators in two-dimensional systems

Huaiyuan Yang(杨怀远), Xi Dai(戴希), and Xin-Zheng Li(李新征)
Chin. Phys. B, 2025, 34 (**9**): 097301. DOI: 10.1088/1674-1056/ade3ae

In-plane negative magnetoresistance and quantum oscillations in van der Waals antiferromagnet $DyTe_3$

Qi Qi(齐琦), Senhao Lv(吕森浩), Ke Zhu(祝轲), Yaofeng Xie(谢耀锋), Guojing Hu(胡国静), Zhen Zhao(赵振), Guoyu Xian(冼国裕), Yechao Han(韩烨超), Yang Yang(杨洋), Lihong Bao(鲍丽宏), Xiao Lin(林晓), Hui Guo(郭辉), Haitao Yang(杨海涛), and Hong-Jun Gao(高鸿钧)
Chin. Phys. B, 2025, 34 (**7**): 077305. DOI: 10.1088/1674-1056/adcc87

Modulating electronic properties of carbon nanotube via constructing one-dimensional vdW heterostructures

Wenqi Lv(吕雯祺), Weili Li(李伟立), Wei Ji(季威), and Yanning Zhang(张妍宁)
Chin. Phys. B, 2025, 34 (**6**): 067303. DOI: 10.1088/1674-1056/adc406

Electronic structure and carrier mobility of BSb nanotubes

Lantian Xue(薛岚天), Chennan Song(宋晨楠), Miaomiao Jian(见苗苗), Qiang Xu(许强), Yuhao Fu(付钰豪), Pengyue Gao(高朋越), and Yu Xie(谢禹)
Chin. Phys. B, 2025, 34 (**3**): 037304. DOI: 10.1088/1674-1056/adacd3

RAPID COMMUNICATION

Strain-enhanced optical gain of hexagonal Ge nanowire

Xue-Li Zhao(赵雪丽)[1,2], Shan Guan(管闪)[1,2,†], Zhigang Song(宋志刚)[3,2], and Jun-Wei Luo(骆军委)[1,2,‡]

[1] *State Key Laboratory of Semiconductor Chip Physics and Technology, Institute of Semiconductors, Chinese Academy of Sciences, Beijing* 100083, *China*
[2] *Center of Materials Science and Optoelectronics Engineering, University of Chinese Academy of Sciences, Beijing* 100049, *China*
[3] *Laboratory of Solid-State Optoelectronics Information Technology, Institute of Semiconductors, Chinese Academy of Sciences, Beijing* 100083, *China*

(Received 28 January 2026; revised manuscript received 4 March 2026; accepted manuscript online 18 March 2026)

The absence of an efficient light source compatible with silicon complementary metal-oxide-semiconductor technology remains a pivotal bottleneck in integrated photonics. Recently, the hexagonal diamond phase of germanium (2H-Ge) has emerged as a promising alternative in light of the direct nature of its bandgap, yet its light emission efficiency falls behind that of III–V semiconductors. Here, by performing theoretical calculations using an atomistic semi-empirical pseudopotential method, we systematically investigate the electronic structure and interband optical gain of [0001]-oriented 2H-Ge nanowires (NWs). We show that quantum confinement in pure 2H-Ge NWs enables diameter-tunable bandgaps across the infrared spectrum, but retains a pseudodirect character with weak near-band-edge optical transitions at the Brillouin zone center. Interestingly, we demonstrate that a moderate uniaxial tensile strain can induce a conduction band inversion, which dramatically enhances the optical gain by over two orders of magnitude and switches the dominant polarization of the emission. We illustrate such an enhancement by correlating the gain characteristics with the energy ordering of the active conduction band states. Our results thus provide essential theoretical guidance and optimization strategies to realize high-performance, polarized light emitters based on 2H-Ge NWs for integrated photonic applications.

Keywords: hexagonal germanium nanowires, uniaxial strain, optical gain, electronic properties

PACS: 73.21.Hb, 42.50.Wk, 42.60.Lh, 73.22.–f

DOI: 10.1088/1674-1056/ae53b7 **CSTR:** 32038.14.CPB.ae53b7

1. Introduction

Since silicon (Si) has achieved remarkable success in the field of microelectronic integrated circuits, Si-based optoelectronics is naturally expected to become an ideal solution for on-chip optical interconnects. However, due to the indirect bandgap nature, radiative transitions in Si between conduction band electrons and valence band holes necessitate phonon assistance, leading to inefficient light emission with a radiative recombination rate typically four to five orders of magnitude lower than that of direct bandgap semiconductors.[1–3] On the other hand, although III–V heterogeneously integrated light sources on Si can currently meet practical application requirements, their incompatibility with the standard complementary metal–oxide–semiconductor (CMOS) process remains a great challenge.[4–9] Therefore, the persistent pursuit of CMOS-compatible Si-based light sources has continued for decades, i.e., exploring avenues such as strain engineering, heterostructures, and nanostructures in Si, germanium (Ge), and their alloys to enhance light emission efficiency.[10–21]

Recently, the metastable hexagonal Lonsdaleite phase of Ge (2H-Ge), which has a direct band gap of around 0.3 eV, has been successfully synthesized experimentally via various methods,[22–29] and was shown to exhibit band-to-band radiative recombination and light emission in 2H-Ge nanostructures,[30,31] 2H-SiGe alloys,[32,33] and quantum well heterostructures,[34] generating intense interest. Unfortunately, the efficiency of light emission for 2H-Ge remains uncompeteable with that of III–V semiconductors due to the weak optical transition strength in spite of a direct band gap.[35–39] Several theoretical proposals, such as alloying,[40–44] strain engineering,[45,46] and heterostructure band alignment,[47] have been put forward to optimize the material characteristics of 2H-Ge for better optical performance. However, most of the proposals have predominantly concentrated on bulk 2H-Ge rather than on nanowire (NW) structures. Notably, low-dimensional nanomaterials possess physical properties distinct from their bulk counterparts because of the presence of quantum confinement effects and interfaces, making them particularly favorable for optoelectronic applications.[48–50] Meanwhile, small-diameter 2H-Ge NWs demonstrate enhanced stability over the cubic phase,[51] which is desirable for miniaturized device applications. Besides, applying strain is more feasible on NWs than on bulk crystals,[52] indicating a higher attainability and effectiveness of strain engineering in low-dimensional structures. Therefore, the investigation of electronic and optical properties of 2H-Ge NWs is urgently needed, particularly for the improvement of optical

†Corresponding author. E-mail: shan_guan@semi.ac.cn
‡Corresponding author. E-mail: jwluo@semi.ac.cn

© 2026 Chinese Physical Society and IOP Publishing Ltd. All rights, including for text and data mining, AI training, and similar technologies, are reserved.

gain.

In this work, we address the above question by exploring the luminescence mechanisms of 2H-Ge NWs. We first reproduce the electronic structures of bulk cubic diamond phase Ge (3C-Ge) and 2H-Ge by employing the semi-empirical pseudopotential method (SEPM), demonstrating the reliability of our calculation method. We then investigate the effects of quantum confinement for 2H-Ge NWs and demonstrate that the band gaps can be effectively reduced with increasing diameter of NWs, approaching the bulk values when the diameter exceeds approximately 10 nm. We further study the optical properties of NWs and show that the optical gain is anisotropic and is tunable by strain. Depending on the orbital characteristics, the energy ordering of the conduction band states functioning in optical gain responds differently to the applied uniaxial strain. Particularly, the dominant optical gain component is switched and can be boosted by over two orders of magnitude at a moderate strain strength (∼4%) with a rather low carrier concentration compared to the unstrained case. Our results reveal strain as an effective mechanism for tuning the optical properties of 2H-Ge NWs to achieve efficient light emission and the associated many fascinating photonic applications.

2. Computation method

The single-particle energy levels ε_i and wave functions ψ_i, corresponding to state i with spin σ for the NWs, are obtained by solving the atomistic semi-empirical pseudopotential Schrödinger equation:[53]

$$\left(-\frac{\hbar^2}{2m}\nabla^2 + V(\boldsymbol{r})\right)\psi_i(\boldsymbol{r},\sigma) = \varepsilon_i\psi_i(\boldsymbol{r},\sigma), \tag{1}$$

where the total potential $V(\boldsymbol{r})$ is constructed as a superposition of screened atomic pseudopotentials $\hat{v}_\alpha$:

$$V(\boldsymbol{r}) = \sum_{n,\alpha}\hat{v}_\alpha(\boldsymbol{r}-\boldsymbol{R}_{n,\alpha}). \tag{2}$$

Here, α denotes the atom type, and $\boldsymbol{R}_{n,\alpha}$ represents the atomic lattice sites. The pseudopotentials $\hat{v}_\alpha$, which include spin-orbit coupling effects and are fitted to experimental data for the diamond structure, are transferable between different polytypes.

The equation is solved numerically in a plane-wave basis. For systems containing a large number of atoms, the folded spectrum method [54] is employed to compute electronic states near the band gap efficiently, avoiding full matrix diagonalization.

To assess the potential performance of NWs as light-emitting devices, the interband optical gain $g_{x,z}$ along the x or z direction (here the y-component is taken to be identical to the x-component, as required by the three-fold rotation operation) is calculated using the expression[55]

$$g_{x,z}(\hbar\omega) = \frac{\pi e^2}{n_{\rm r}c\varepsilon_0 m_0^2\omega}\cdot\frac{1}{V}\sum_{c,v}\sum_{\boldsymbol{k}}|M_{cv}^{x,z}|^2 \times\left[f_c(\boldsymbol{k})-f_v(\boldsymbol{k})\right]\delta\left[E_{cv}(\boldsymbol{k})-\hbar\omega\right], \tag{3}$$

where $n_{\rm r}$, c, ε_0, m_0, and V represent the refractive index, the speed of light in vacuum, the vacuum permittivity, the free-electron mass, and the volume, respectively. The calculation considers only vertical interband transitions near the band edges, neglecting intervalley scattering and indirect optical transitions involving phonon assistance. The transition energy is $E_{cv}(\boldsymbol{k}) = E_c(\boldsymbol{k}) - E_v(\boldsymbol{k})$, with the momentum matrix element given by $M_{cv}^{x,z} = \langle\psi_{c\boldsymbol{k}}|p_{x,z}|\psi_{v\boldsymbol{k}}\rangle$ for transitions from conduction band c to valence band v, where $p_{x,z}$ stands for x,z-component of the momentum operator $\hat{p}$. The corresponding Kane energy, which characterizes the optical transition strength, is proportional to the square of the momentum matrix element:[56]

$$E_{\rm p}^{x,z} = \frac{2}{m_0}|M_{cv}^{x,z}|^2. \tag{4}$$

The total Kane energy is then obtained by summing over all polarization components:

$$E_{\rm p} = E_{\rm p}^x + E_{\rm p}^y + E_{\rm p}^z. \tag{5}$$

Carrier occupation is described by the Fermi–Dirac distribution for electrons, $f_c(\boldsymbol{k})$, and holes, $1-f_v(\boldsymbol{k})$, where the corresponding quasi-Fermi levels are denoted as $E_{\rm fc}$ and $E_{\rm fv}$, respectively:

$$f_c(\boldsymbol{k}) = \frac{1}{1+\exp\left(\dfrac{E(\boldsymbol{k})-E_{\rm fc}}{k_{\rm B}T}\right)},$$
$$1-f_v(\boldsymbol{k}) = \frac{1}{1+\exp\left(\dfrac{E_{\rm fv}-E(\boldsymbol{k})}{k_{\rm B}T}\right)}, \tag{6}$$

where $k_{\rm B}$ is the Boltzmann constant. These quasi-Fermi levels are determined numerically at a given temperature T from the conduction and valence band density of states (DOS) ($D_c(E)$ and $D_v(E)$) obtained by counting the states within a small energy window and the prescribed carrier concentrations n and p (under charge neutrality, $n = p$) via the equations

$$n = \int_{E_{\rm CBM}}^{\infty} D_c(E)f_c(E)\,{\rm d}E, \tag{7}$$

$$p = \int_{-\infty}^{E_{\rm VBM}} D_v(E)\left[1-f_v(E)\right]{\rm d}E, \tag{8}$$

where $E_{\rm CBM}$ and $E_{\rm VBM}$ denote the energies of the conduction band minimum (CBM) and valence band maximum (VBM), respectively.

In the numerical evaluation of Eq. (3), the Dirac delta function is replaced by the broadening function of $\mathcal{L}(E_{cv}-$

$\hbar\omega) = \frac{1}{\gamma\pi}\,\mathrm{sech}\left(\frac{E_{cv}-\hbar\omega}{\gamma}\right)$, which provides a more physical representation of spectral broadening than a conventional Lorentzian lineshape.[57] A broadening parameter of $\gamma =$ 10 meV is used throughout this work, and all calculations are performed at $T = 300$ K.

3. Results and discussion

3.1. Band structures for bulk 3C-Ge and 2H-Ge

Conventional 3C-Ge crystallizes in the cubic diamond structure with space group $Fd\bar{3}m$, exhibiting that the atomic bilayers in the hexagonal unit cells stack along the [0001] direction with an ABCABC pattern, as illustrated in Fig. 1(a). In contrast, 2H-Ge possesses an ABAB arrangement, belonging to the space group $P6_3/mmc$ (see Fig. 1(b)). 3C-Ge is defined by a single lattice constant $a_0 = 5.6579$ Å, whereas the 2H-Ge unit cell is characterized by the lattice parameters a and c, along with an internal coordinate u, which for the ideal crystal structure are $a = 4.0007$ Å, $c = 6.5332$ Å, and $u = 3/8$, respectively. The electronic band structures of 2H-Ge and 3C-Ge, calculated using SEPM with spin-orbit coupling included, are presented in Figs. 1(c) and 1(d), respectively. We see that 3C-Ge shows an indirect band gap of 0.762 eV with the CBM located at the L point, whereas the VBM is at the Γ point. For 2H-Ge, it possesses a direct bandgap at the Γ point of about 0.227 eV. One also observes that all the bands are doubly degenerate due to the preserved inversion symmetry. The calculated band structures compare well with the reported optical bandgap and exhibit excellent agreement with the results reported by Rödl *et al.*,[37] demonstrating the validity of our used SEPM method.

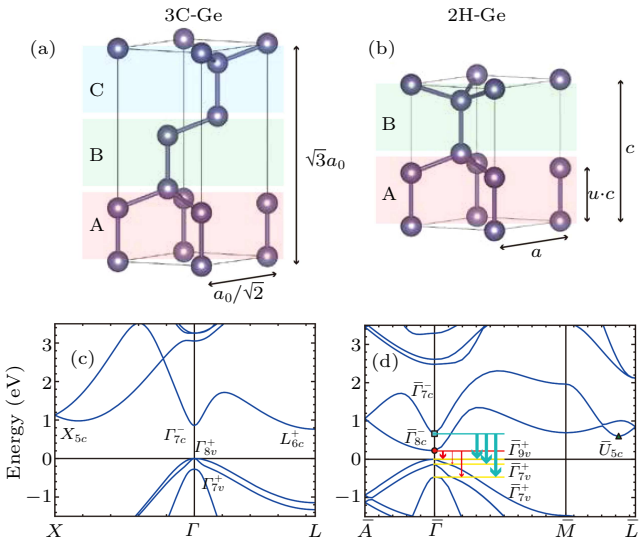


Fig. 1. Atomic bilayer stacking along the [0001] direction in the hexagonal unit cells of (a) 3C-Ge and (b) 2H-Ge. Calculated band structures of the primitive cell for (c) 3C-Ge along the X–Γ–L path and (d) 2H-Ge along the $\bar{A}$–$\bar{\Gamma}$–$\bar{M}$–$\bar{L}$ path. The VBM is set to zero. Double-group irreducible representations of the band-edge states are indicated. Arrows in (d) illustrate the transitions between the three highest valence bands and the two lowest conduction bands in 2H-Ge, with the line thickness indicating the relative transition strength.

Of particular relevance to the optical properties are the band edge states. For simplicity, we label these states using the double-group irreducible representation notation of Koster *et al.*,[58] where the superscripts + and − denote even and odd parity under inversion symmetry, respectively, and the subscripts v and c indicate valence and conduction band character. High-symmetry points in the 2H phase are distinguished from those of the 3C phase by an overbar notation. The CBM of 3C-Ge at the L valley (L^+_{6c}) folds in part into the $\bar{\Gamma}$ point in 2H-Ge. Strong repulsive L–L interaction splits the states into higher and lower energy levels, with the lower one forming the first conduction band state $\bar{\Gamma}^-_{8c}$, at 0.227 eV, which also constitutes the CBM of 2H-Ge. The remaining equivalent L points, together with the X points, map to the $\bar{U}$ point along the $\bar{M}$–$\bar{L}$ path, lying approximately two-thirds of the way from $\bar{M}$ to $\bar{L}$. The resulting $\bar{U}_{5c}$ state in 2H-Ge exhibits an energy of 0.604 eV, nearly equal to the average of the X_{5c} and L^+_{6c} state energies in 3C-Ge.[38,59] In addition, the Γ valley of 3C-Ge, corresponding to Γ^-_{7c}, becomes the second conduction band state $\bar{\Gamma}^-_{7c}$ in 2H-Ge, with an eigenenergy of 0.669 eV. This energy level remains unaffected because the inversion symmetry forbids repulsion with the VBM, which contrasts with compound semiconductors.[38] Regarding the valence band, crystal field splitting and spin–orbit coupling jointly lift the valence band degeneracy at $\bar{\Gamma}$ in 2H-Ge, resulting in three distinct states: $\bar{\Gamma}^+_{9v}$, $\bar{\Gamma}^+_{7v}$, and $\bar{\Gamma}^+_{7v}$ with energies of 0 eV, −0.129 eV, and −0.457 eV, respectively. Although both the VBM and CBM are located at the $\bar{\Gamma}$ point in 2H-Ge, in contrast to the indirect band gap of 3C-Ge, the interband transition ($\bar{\Gamma}^-_{8c}$ to $\bar{\Gamma}^+_{9v}$) remains several orders of magnitude weaker than that of a true direct band gap semiconductor.[60,61] This renders 2H-Ge a pseudodirect band gap material. Nevertheless, the interband transition between the second conduction band state $\bar{\Gamma}^-_{7c}$ and the valence band states is much stronger, implying the possibility of improving the optical properties by band engineering.

3.2. Quantum confinement effects in 2H-Ge NW

We then investigate the quantum confinement effect on 2H-Ge by focusing on its NW structure. The inset of Fig. 2(a) displays a structural model of a $d = 4$ nm 2H-Ge NW oriented along the [0001] direction with a regular hexagonal cross-section, where the diameter d is defined as the diagonal length of the hexagon. To eliminate in-gap surface states, the NW is embedded in an artificial lattice-matched barrier material that passivates the surface dangling bonds; the passivating pseudoatoms are omitted for clarity in the illustration. Generally, surface states and defects are detrimental to emission. However, for 2H-Ge NWs, the dominant I_3-type stacking faults do not introduce states within the band gap.[62] And the low surface recombination[63] combined with effective passi-

vation strategies[64] mitigates the surface impact. Our ideal model thus simulates a best-case scenario, corresponding to a high-quality 2H-Ge NW grown on a thin GaAs core using the crystal transfer method,[32] which minimizes lattice mismatch and strain-induced defects. This $d = 4$ nm NW is chosen as a representative system for studying the electronic and optical properties of 2H-Ge NWs due to its pronounced quantum confinement and lower formation energy compared to the 3C polytype.[51]

Figure 2(a) shows the calculated band structure near the band gap along the $\overline{\Gamma}$–$\overline{A}$ path. One observes that both the VBM and CBM reside at $\overline{\Gamma}$ with a direct band gap of 0.885 eV. Since the main symmetry operations are retained at $\overline{\Gamma}$, we label the relevant conduction band states as $\overline{L'}$, $\overline{\Gamma'}$, and $\overline{X'}$, as evolved from the bulk states. The valence subbands are labeled as v_1, v_2, v_3, etc., in order of decreasing energy at the $\overline{\Gamma}$ point. The conduction band around $\overline{\Gamma'}$ shows an ideal parabolic s-like band behavior with a higher dispersion than that around $\overline{L'}$, whereas the valence band exhibits non-parabolic behavior that is attributed to the coupling between valence subbands.

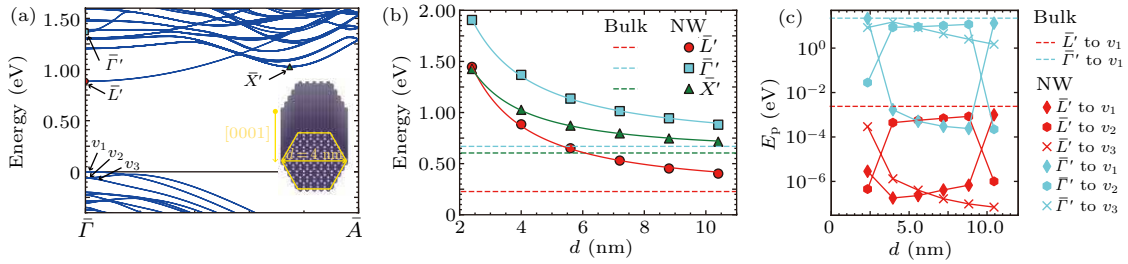


Fig. 2. (a) Calculated band structure for a [0001]-oriented 2H-Ge NW with a diameter of $d = 4$ nm. The inset shows the atomistic model with passivating pseudoatoms omitted. The evolution of energy levels (b) and the optical transition strength (total Kane energy) (c) for active band states as a function of the d in 2H-Ge NWs. The $\overline{L'}$, $\overline{\Gamma'}$, and $\overline{X'}$ states in NWs are marked by red circles, cyan squares, and green triangles, respectively. Dashed lines show bulk counterparts.

The degree of quantum confinement effect depends on the NW diameter, which can engineer the band edge energies and the resulting band gap. We thus extract the energy levels of the $\overline{L'}$, $\overline{\Gamma'}$, and $\overline{X'}$ states for NWs with different diameters and plot the results in Fig. 2(b). All energies are referenced to the VBM of the NW at each respective diameter. We find that, as the diameter increases, the band gap decreases, resulting in a red shift of both absorption and emission edges in NWs. The band gap of 2H-Ge NWs follows a power-law dependence on diameter,[48,65] described by $E_{\mathrm{NW}} = E_{\mathrm{bulk}} + Cd^{-\alpha}$, with fitted parameters $C = 3.726$ and $\alpha = 1.270$. For large diameters, we see that quantum confinement becomes negligible and the band gap approaches the bulk value. This enables tuning of the emission energy from approximately 1.4 eV to 0.3 eV by varying the NW diameter, covering a broad range relevant for infrared optoelectronic applications. On the other hand, as the diameter is reduced, these three conduction states, $\overline{L'}$, $\overline{\Gamma'}$, and $\overline{X'}$, all increase, but at different rates. The energy difference $\Delta E_{\mathrm{RD}} = E(\overline{\Gamma'}) - E(\overline{L'})$ remains nearly constant, indicating that the relative positions of the $\overline{L'}$ and $\overline{\Gamma'}$ states cannot be effectively tuned by size reduction alone. In contrast, the indirect character $\Delta E_{\mathrm{ID}} = E(\overline{X'}) - E(\overline{L'})$ decreases with decreasing diameter and becomes negative for diameters below 2.4 nm. In this regime, the NW becomes an indirect band gap semiconductor, with the $\overline{X'}$ state lying 0.021 eV below $\overline{L'}$ at $d = 2.4$ nm.

The characteristic that the energy of the $\overline{\Gamma'}$ state remains higher than that of $\overline{L'}$ for different diameters indicates a pseudodirect band gap nature in 2H-Ge NW. This is corroborated by the calculated interband transition matrix elements using Eq. (4) in Fig. 2(c). It shows the dependence of transitions from the conduction states $\overline{L'}$ and $\overline{\Gamma'}$ to the three highest valence subband states v_1, v_2, v_3 at the $\overline{\Gamma}$ point on different NW diameters. For comparison, dashed lines indicate transitions to the VBM in bulk 2H-Ge. One observes that the transition strength from the $\overline{\Gamma'}$ state to specific valence subbands approaches that of canonical true direct-bandgap semiconductors, e.g., 28.8 eV for GaAs,[60] exceeding transitions from the $\overline{L'}$ state by two to three orders of magnitude. This substantial disparity means intrinsically low interband luminescence efficiency. Consequently, the interband luminescence efficiency is fundamentally limited by these small band edge transitions.

3.3. Optical gain for 2H-Ge NW

We next plot the DOS in Fig. 3(a), which exhibits sharp peaks in both the valence and conduction bands within a relatively low energy range. The quasi-Fermi levels can be determined from the DOS and carrier concentration according to Eqs. (6) and (8) for a given temperature. Figure 3(b) presents the quasi-Fermi levels E_{fc} and E_{fv} as a function of electron and hole concentrations n and p, respectively, at $T = 300$ K under zero doping conditions. Here, $n_0 = 1 \times 10^{18}$ cm^{-3} is used as the unit carrier concentration. In the absence of doping, where the donor and acceptor concentrations (N_{d} and N_{a}) are zero, the general relations $n = N_{\mathrm{d}} + \Delta n$ and $p = N_{\mathrm{a}} + \Delta n$ simplify to $n = p = \Delta n$. Thus, the injected carrier concentration Δn dominates the carrier concentrations. We see that, at $\Delta n = 5n_0$, E_{fc} resides at approximately 0.864 eV, remaining below the CBM, while E_{fv} lies at about 0.030 eV, above the VBM. When the concentration increases to $20n_0$, E_{fc} reaches 0.928 eV and

enters the conduction band, whereas E_{fv} shifts to -0.018 eV, crossing the valence band. Under this condition, population inversion is achieved, with electrons primarily occupying the $\overline{L'}$ state at $\overline{\Gamma}$. At $\Delta n = 65n_0$, E_{fc} further increases to 1.028 eV and E_{fv} decreases to -0.106 eV, leading to partial occupation of the indirect $\overline{X'}$ valley at 1.026 eV.

Having obtained the DOS along with the quasi-Fermi levels for 2H-Ge NWs, we then evaluate the optical gain $g(E)$, which is an important parameter for measuring the performance of a laser. The optical gain $g(E)$ is computed using Eq. (3), taking into account only vertical interband transitions between the 10 lowest conduction bands and 10 highest valence bands. Owing to the weak transition strength of the z-component near the band edges, its contribution to the gain component g_z is positive yet negligible. Therefore, only the gain spectra along the x-direction under various injected carrier concentrations Δn are presented in Fig. 3(c). Generally, the NW obtains a positive gain component g_x when the carrier injection concentration is about $20n_0$, and it continues to be enhanced with increasing concentration. The g_x spectrum exhibits a single peak near 935 meV, originating from $\overline{L'}$-to-v_2 transition. Notably, this energy exceeds the 886 meV band gap associated with $\overline{L'}$-to-v_1 transition, which does not contribute visibly to the gain. In larger-diameter NWs, the electron and hole states become dense, which may lead to more complex gain spectra featuring multiple peaks.

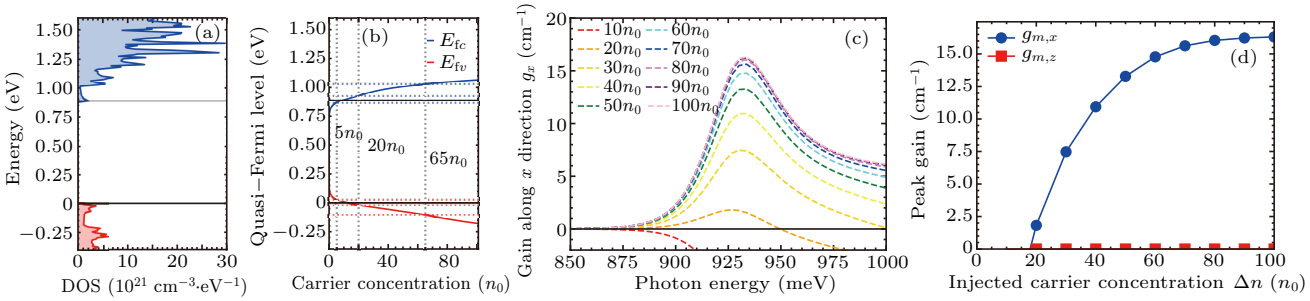


Fig. 3. (a) DOS. (b) Quasi-Fermi levels E_{fc} and E_{fv} as a function of the carrier concentrations n and p. (c) Optical gain spectra for x-components. (d) Peak gain versus injected carrier concentration Δn. The diameter d of 2H-Ge NW is set to be 4 nm. Results are obtained at $T = 300$ K and Δn is given in units of $n_0 = 1 \times 10^{18}$ cm^{-3}.

Figure 3(d) shows the peak gain g_m for the z- and x-polarization components as a function of Δn. $g_{m,x}$ consistently exceeds $g_{m,z}$ at any given injection level, confirming the polarized nature of the emission. Compared with cubic Ge NWs, which exhibit no positive optical gain even at injected carrier densities up to $40n_0$ [16] due to their indirect band structure, the positive gain in 2H-Ge NW emerges around $\Delta n = 20n_0$. Furthermore, a distinct trend is observed: the peak gain rises with the injection electron concentration and eventually saturates. This saturation, which reaches about 17 cm^{-1} for g_x at high injection beyond $65n_0$, is attributed to the occupation of indirect $\overline{X'}$ valleys and represents a limiting factor for light-emission efficiency.

3.4. Strain-enhanced gain spectra for 2H-Ge NW

Although light emission is achievable, the relatively high threshold carrier concentration required for positive optical gain and the weak emission intensity are limiting factors. This renders small pure 2H-Ge NWs suboptimal for highly efficient light-emitting applications. Strain has long been known as an effective mechanism for tuning photoelectric properties of semiconductors, which is particularly useful for low dimensional systems thanks to the sustainability of larger strains than their bulk crystals. Figure 4(a) illustrates the evolution of relevant conduction band state energies relative to the VBM in a $d = 4$ nm 2H-Ge NW under uniaxial tensile strain ε_z applied along the [0001] direction. With increasing strain, the states $\overline{L'}$ and $\overline{\Gamma'}$ respond differently to strain: $\overline{\Gamma'}$ is pulled down while $\overline{L'}$ is pushed up, partially due to their different bonding characters. Band inversion between $\overline{L'}$ and $\overline{\Gamma'}$ occurs just above 3% strain. Meanwhile, the $\overline{X'}$ state is insensitive to strain, which becomes the lowest conduction state at ε_z from 2.2% to 3.7%, resulting in an indirect bandgap. A true direct bandgap, with $\overline{\Gamma'}$ as the CBM, is achieved at approximately 4% strain, which is within the experimentally available range for low-dimensional materials.[65,66] Such a transition implies that a significantly-enhanced optical gain can be realized at a relatively low carrier concentration for strained NWs.

The corresponding optical gain spectra under these strains are shown in Fig. 4(b). The spectra clearly show that they resemble the unstrained case but exhibit a blue-shifted gain peak due to the elevated $\overline{L'}$ state at a 1% or 2% strain. At a 2% strain, the $\overline{X'}$ and $\overline{L'}$ states become nearly aligned, leading to simultaneous carrier filling and thus a significant increase in the carrier concentration threshold for positive gain from approximately $20n_0$ to $35n_0$. At $\varepsilon_z = 3\%$, carriers initially populate the $\overline{X'}$ state prior to occupying $\overline{L'}$ and $\overline{\Gamma'}$, further raising the threshold to about $45n_0$ and inducing a blue shift in the gain peak. The energy proximity between $\overline{L'}$ and $\overline{\Gamma'}$ under this condition drives the optical gain to arise predominantly from $\overline{\Gamma'}$-to-VBM transitions. These transitions exhibit polarization characteristics distinct from those associated with $\overline{L'}$. At $\Delta n = 50n_0$, the peak gain reaches ~ 170 cm^{-1} for the x-component and ~ 5200 cm^{-1} for the z-component, scaling nearly linearly with

further carrier injection. This behavior stands in stark contrast to the $\overline{L}'$-dominated regime, where $g_x \gg g_z$ and peak gains are typically limited to tens cm^{-1}. At $\varepsilon_z = 4\%$, $\overline{X}'$ and $\overline{\Gamma}'$ become nearly equal, causing carriers to populate both states and reducing the threshold carrier concentration to approximately $10n_0$. At $\Delta n = 12n_0$, the peak gain is ~ 6400 cm^{-1} for the z-component, which is ~ 60-fold larger than the x-component (~ 110 cm^{-1}). As $\overline{\Gamma}'$ descends to become the CBM, transitions from $\overline{\Gamma}'$ to the valence band dominate the gain spectrum, resulting in a red-shifted gain peak and a rapid increase in optical gain with rising carrier injection. This trend continues at a 5% strain, where a further lowering of $\overline{\Gamma}'$ results in an additional red shift and a remarkably low threshold, enabling efficient light emission with g_z attaining ~ 6700 cm^{-1} even at $\Delta n = 3n_0$.

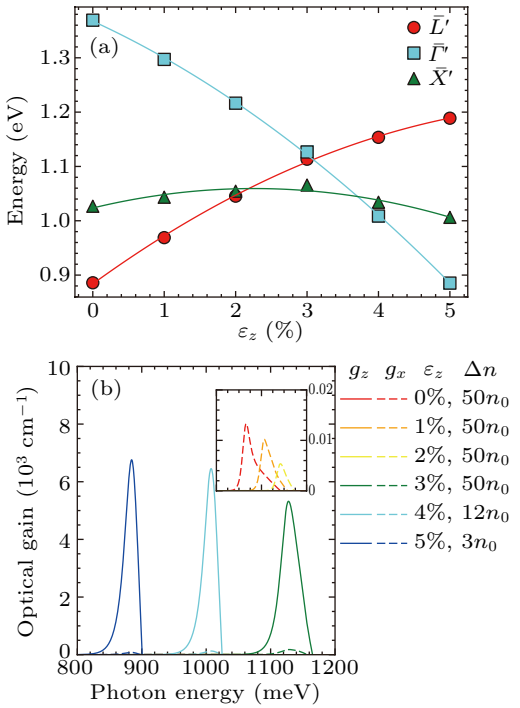


Fig. 4. (a) Strain-dependent energy evolution of conduction band states and (b) corresponding optical gain spectra for a $d = 4.0$ nm 2H-Ge NW under uniaxial strain ε_z along the [0001]-direction. All gain spectra are calculated at $T = 300$ K and Δn is given in units of $n_0 = 1 \times 10^{18}$ cm^{-3}.

For carrier concentrations of $\sim 10^{18}$–10^{19} cm^{-3}, free-carrier absorption (FCA) losses are estimated at 500–2000 cm^{-1}.[16,33,68,69] After accounting for these losses, the net gain of our strain-enhanced 2H-Ge NWs still reaches several thousand cm^{-1}, which is sufficient for lasing. The above discussion considers undoped NWs. In experiments, however, n-type doping of 2H-Ge is commonly employed.[31,32] Heavy n-type doping provides a carrier reservoir near the active states, further lowering the lasing threshold. Nevertheless, it also increases FCA losses and ionized impurity scattering, which can partially offset the gain enhancement. Hence, practical device optimization requires a careful balance between these factors.

Therefore, the gain characteristics can be directly correlated with the relative energy ordering of the $\overline{L}'$, $\overline{X}'$, and $\overline{\Gamma}'$ states. The peak gain magnitude is primarily determined by the competition between $\overline{L}'$ and $\overline{\Gamma}'$. When $\overline{\Gamma}'$ lies below or close to $\overline{L}'$, strong $\overline{\Gamma}'$-to-valence band transitions yield a high gain with pronounced polarization $g_z > g_x$, suitable for efficient light-emitting devices. Otherwise, gain is limited by the weaker matrix elements of $\overline{L}'$-based transitions, accompanied by $g_x \gg g_z$. The spectral position of the gain peak corresponds to the dominant transition energy. The threshold carrier density is strongly influenced by the indirect $\overline{X}'$ state: when $\overline{X}'$ lies below or approaches the zone-center CBM in energy, whether $\overline{L}'$ or $\overline{\Gamma}'$, carriers preferentially or partially occupy this state, thereby raising the injection level required for population inversion and positive gain. The mechanism elucidated here is generalizable to other systems with multi-valley bands, such as 3C-Ge,[16] GeSn alloys,[70] 2H-SiGe alloys,[33] or heterostructures[57] (e.g., quantum wells, cascade lasers), where strain engineering can induce band inversion for enhanced gain.

The two-to-three-order-of-magnitude enhancement in optical gain triggered by band inversion is a universal feature of 2H-Ge NWs, independent of diameter. The underlying mechanism is that the intrinsic transition strengths associated with the $\overline{L}'$ and $\overline{\Gamma}'$ states exhibit no significant variation with either strain or diameter. Specifically, the transition strength E_p for transitions from the $\overline{L}'$ and $\overline{\Gamma}'$ states to the valence band edge states is on the order of 10^0–10^1 eV and 10^3–10^4 eV, respectively. Consequently, once the strain is sufficient to switch the dominant transition from the $\overline{L}'$ state to the $\overline{\Gamma}'$ state, this magnitude of gain enhancement is universally realized.

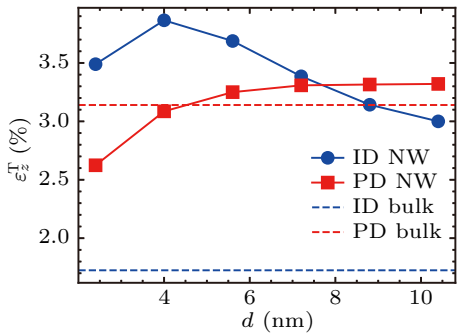


Fig. 5. The evolution of critical strain ε_z^T for band inversion as a function of the d in 2H-Ge NWs. Red squares and blue circles represent the strains required for the $\overline{L}'$ to $\overline{\Gamma}'$ transition (PD) and for the $\overline{X}'$ to $\overline{\Gamma}'$ transition (ID) in NWs. Dashed lines indicate the corresponding critical strains for bulk 2H-Ge.

We further examine the size dependence of the critical optimal strain, which involves the relative magnitudes of the pseudo-to-direct transition strain (PD) and the indirect-to-direct transition strain (ID). Figure 5 presents the extracted transition strains ε_z^T (%) as a function of diameter for both bulk and NWs of 2H-Ge. We see that, in the small-diameter

regime ($d < 7.2$ nm), PD increases gradually with increasing diameter, with the rate of increase slowing as the diameter grows. As the diameter further increases, PD is expected to gradually decrease and converge toward the bulk PD value of approximately 3%. In contrast, ID decreases progressively with increasing diameter for diameters above 4 nm, and then converges toward the bulk ID value (below 2%). In the small-diameter regime ($d < 7.2$ nm), ID consistently exceeds PD, and thus ID is identified as the critical optimal strain. Within the diameter range of 4–7.2 nm, ID decreases as the diameter increases, with the maximum critical optimal strain of approximately 4% occurring at $d = 4$ nm. For diameters larger than 7.2 nm, PD is expected to exceed ID, making PD the critical optimal strain, with a value of approximately 3.2%. Therefore, for 2H-Ge NWs of any diameter, the application of a uniaxial tensile strain in the range of 3%–4% is sufficient to achieve efficient light emission.

4. Conclusion

We point out that previous studies have demonstrated that strain engineering in bulk 2H-Ge can induce a band inversion between the first ($\overline{\Gamma}^{-}_{8c}$) and second ($\overline{\Gamma}^{-}_{7c}$) conduction bands, transforming the material from a pseudodirect to a true direct bandgap semiconductor.[44–46] However, for bulk 2H-Ge, this transition requires the application of a hydrostatic tensile strain of approximately 6% or, alternatively, a uniaxial tensile strain of approximately 2% along the z-axis.[45] For NWs, the expected 3%–4% tensile strain required for band inversion is difficult to achieve via lattice mismatch alone in core/shell heterostructures. Such strains are more readily obtained through external methods such as microelectromechanical systems (MEMS),[71–73] piezomanipulator tips,[74,75] and flexible substrates.[52,76] In spite of the availability of such strains in an experimental setup, their long-term reliability after device packaging remains a challenge, which deserves a further study.

Experimental validation of our predictions will require the synthesis of high-quality 2H-Ge NWs with controlled diameters, followed by the application of uniaxial tensile strain using MEMS or flexible substrates.[66] Key experimental signatures include a sharp increase and polarization switching in photoluminescence upon band inversion, and direct measurement of enhanced optical gain.[33] These observable features will serve as a valuable guide for future experimental efforts toward realizing efficient 2H-Ge NW-based light sources.

In conclusion, we have conducted a detailed computational study using the SEPM method to evaluate the potential of 2H-Ge NWs as efficient light sources for Si-integrated photonics. The diameter-dependent evolution of key conduction band states, $\overline{L}'$, $\overline{\Gamma}'$, $\overline{X}'$ in unstrained [0001]-oriented 2H-Ge NWs is revealed. Although quantum confinement enables effective bandgap tuning across the infrared spectrum from 0.3 eV to 1.4 eV, the associated interband transitions remain so weak that a high carrier injection is required to achieve positive optical gain. We identify uniaxial tensile strain along the [0001] axis as a powerful means to dramatically tailor the band structure and optical response. As the applied strain increases from 0% to 5%, the NWs undergo a sequence of transitions: from a pseudodirect gap, through an indirect gap at $\sim 2\%$ strain, to a true direct-gap semiconductor at a critical strain of $\sim 4\%$. Correspondingly, the gain spectrum exhibits a characteristic blue-shift followed by a red-shift with increasing strain, accompanied by a band inversion that occurs between the $\overline{L}'$ and $\overline{\Gamma}'$. Such a band inversion triggers a profound enhancement in optical gain: the peak gain increases by more than two orders of magnitude, and the emission becomes polarized along the NW axis ($g_z > g_x$). These results establish a clear strain-engineering pathway toward efficient light emission based on 2H-Ge NWs.

Acknowledgements

The work is supported by the National Key R&D Program of China (Grant No. 2024YFA1408200), the National Natural Science Foundation of China (Grant Nos. 12525402 and 12374078), and the CAS Project for Young Scientists in Basic Research (Grant Nos. YSBR-120 and YSBR-026).

References

[1] Semyonov O, Subashiev A, Chen Z and Luryi S 2010 *J. Appl. Phys.* **108** 13101
[2] Lush G B 2009 *Sol. Energy Mater. Sol. Cells* **93** 1225
[3] Trupke T, Green M A, Würfel P, Altermatt P P, Wang A, Zhao J and Corkish R 2003 *J. Appl. Phys.* **94** 4930
[4] Zhou Z, Yin B and Michel J 2015 *Light: Sci. Appl.* **4** e358
[5] Han Y, Park H, Bowers J and Lau K M 2022 *Adv. Opt. Photonics* **14** 404
[6] Zhou Z, Ou X, Fang Y, Alkhazraji E, Xu R, Wan Y and Bowers J E 2023 *Elight* **3** 1
[7] Wei W Q, He A, Yang B, Wang Z H, Huang J Z, Han D, Ming M, Guo X, Su Y, Zhang J J and Wang T 2023 *Light: Sci. Appl.* **12** 84
[8] Ting W, Zhang J J and Liu H Y 2015 *Acta Phys. Sin.* **64** 204209 (in Chinese)
[9] Wei W Q, Wang J H, Zhang J Y, Feng Q, Wang Z, Xu H X, Wang T and Zhang J J 2020 *Chin. Phys. Lett.* **37** 24203
[10] El Kurdi M, Fishman G, Sauvage S and Boucaud P 2010 *J. Appl. Phys.* **107** 13710
[11] Gnutzmann U and Clausecker K 1974 *Appl. Phys.* **3** 9
[12] Menczigar U, Abstreiter G, Olajos J, Grimmeiss H, Kibbel H, Presting H and Kasper E 1993 *Phys. Rev. B* **47** 4099
[13] d'Avezac M, Luo J W, Chanier T and Zunger A 2012 *Phys. Rev. Lett.* **108** 27401
[14] Zhang L, d'Avezac M, Luo J W and Zunger A 2012 *Nano Lett.* **12** 984
[15] Ji Z M, Luo J W and Li S S 2020 *New J. Phys.* **22** 93037
[16] Xiong W, Wang J W, Fan W J, Song Z G and Tan C S 2020 *Sci. Rep.* **10** 32
[17] Yuan L D, Li S S and Luo J W 2024 *Nat. Commun.* **15** 618
[18] Ming M, Gao F, Wang J H, Zhang J Y, Wang T, Yao Y, Hu H and Zhang J J 2023 *Nanoscale* **15** 7311
[19] Scappucci G, Kloeffel C, Zwanenburg F A, Loss D, Myronov M, Zhang J J, De Franceschi S, Katsaros G and Veldhorst M 2021 *Nat. Rev. Mater.* **6** 926
[20] Wang J H, Ming M, Huang D M, Zhang J Y, Luo Y, Fu B X, Chu Y X, Yao Y, Xu H and Zhang J J 2025 *Nano Lett.* **25** 11125

[21] Zhang J J, Katsaros G, Montalenti F, Scopece D, Rezaev R O, Mickel C, Rellinghaus B, Miglio L, De Franceschi S, Rastelli A and Schmidt O G 2012 *Phys. Rev. Lett.* **109** 85502

[22] Zhang Y, Iqbal Z, Vijayalakshmi S, Qadri S and Grebel H 2000 *Solid State Commun.* **115** 657

[23] Vincent L, Patriarche G, Hallais G, Renard C, Gardès C, Troadec D and Bouchier D 2014 *Nano Lett.* **14** 4828

[24] Hauge H I T, Conesa-Boj S, Verheijen M A, Koelling S and Bakkers E P A M 2017 *Nano Lett.* **17** 85

[25] Ilkiv I V, Kotlyar K P, Kirilenko D A, Osipov A V, Soshnikov I P, Mikushev S V, Dubrovskii V G and Cirlin G E 2021 *ACS Appl. Nano Mater.* **4** 7289

[26] Serghiou G, Odling N, Reichmann H J, Ji G, Koch-Müller M, Frost D J, Wright J P, Boehler R and Morgenroth W 2021 *Chem. Eur. J.* **27** 14217

[27] Li A, Hauge H I T, Verheijen M A, Bakkers E P A M, Tucker R T, Vincent L and Renard C 2022 *Nanotechnology* **34** 15601

[28] Dudko I, Dursap T, Lamirand A D, Botella C, Regreny P, Danescu A, Brottet S, Bugnet M, Walia S, Chauvin N and Penuelas J 2022 *Cryst. Growth Des.* **22** 32

[29] Wang X, Kaufmann R, Jones A C, Chen R, Ahmed T, Pettes M T, Kotula P G, Bilgin I, Wang Y, Kar S and Yoo J 2023 *Mater. Today Adv.* **19** 100401

[30] Zhang N, Yan J, Wang L, Zhang J, Zhang Z, Miao T, Zheng C, Jiang Z, Hu H and Zhong Z 2024 *ACS Nano* **18** 328

[31] Van Lange V T, Dijkstra A, Fadaly E M T, Peeters W H J, Van Tilburg M A J, Bakkers E P A M, Bechstedt F, Finley J J and Haverkort J E M 2024 *ACS Photonics* **11** 4258

[32] Fadaly E M T, Dijkstra A, Suckert J R, Ziss D, Van Tilburg M A J, Mao C, Ren Y, Van Lange V T, Korzun K, Kölling S, Verheijen M A, Busse D, Rödl C, Furthmüller J, Bechstedt F, Stangl J, Finley J J, Botti S, Haverkort J E M and Bakkers E P A M 2020 *Nature* **580** 205

[33] Van Tilburg M A J, Farina R, Van Lange V T, Peeters W H J, Meder S, Jansen M M, Verheijen M A, Vettori M, Finley J J, Bakkers Erik P A M and Haverkort Jos E M 2024 *Commun. Phys.* **7** 328

[34] Peeters W H J, Van Lange V T, Belabbes A, Van Hemert M C, Jansen M M, Farina R, Van Tilburg M A J, Verheijen M A, Botti S, Bechstedt F, Haverkort Jos E M and Bakkers E P A M 2024 *Nat. Commun.* **15** 5252

[35] Tizei L H G, Fiorentin M R, Dursap T, van den Berg T M, Túnica M, Palummo M, Kociak M, Vincent L and Amato M 2025 *Nano Lett.* **25** 8604

[36] De A and Pryor C E 2014 *J. Phys.: Condens. Matter* **26** 45801

[37] Rödl C, Furthmüller J, Suckert J R, Armuzza V, Bechstedt F and Botti S 2019 *Phys. Rev. Mater.* **3** 34602

[38] Cai X, Deng H X and Wei S H 2021 *Phys. Rev. B* **103** 245202

[39] Pulcu Y, Koltai J, Kormányos A and Burkard G 2024 *Phys. Rev. B* **109** 205202

[40] Cartoixà X, Palummo M, Hauge H I T, Bakkers E P A M and Rurali R 2017 *Nano Lett.* **17** 4753

[41] Borlido P, Suckert J R, Furthmüller J, Bechstedt F, Botti S and Rödl C 2021 *Phys. Rev. Mater.* **5** 114604

[42] Bao N, Guo F, Kang D, Feng Y, Wang H and Dai J 2021 *J. Appl. Phys.* **129** 145701

[43] Wang Z, Zhang Z, Liu S, Robertson J and Guo Y 2021 *Appl. Phys. Lett.* **118** 172101

[44] Belabbes A, Bechstedt F and Botti S 2022 *Phys. Status Solidi – Rapid Res. Lett.* **16** 2100555

[45] Suckert J R, Rödl C, Furthmüller J, Bechstedt F and Botti S 2021 *Phys. Rev. Mater.* **5** 24602

[46] Mayengbam R, Tan C S and Weijun Fan 2023 *RSC Adv.* **13** 11324

[47] Belabbes A, Keller M, Furthmüller J, Botti S and Bechstedt F 2025 *Phys. Rev. B* **112** 205304

[48] Rurali R 2010 *Rev. Mod. Phys.* **82** 427

[49] Notomi M, Takiguchi M, Sergent S, Zhang G and Sumikura H 2020 *Opt. Mater. Express* **10** 2560

[50] Singh S, Das S and Ray S K 2023 *Appl. Phys. A* **129** 216

[51] Scalise E, Sarikov A, Barbisan L, Marzegalli A, Migas D, Montalenti F and Miglio L 2021 *Appl. Surf. Sci.* **545** 148948

[52] Smith D A, Holmberg V C and Korgel B A 2010 *ACS Nano* **4** 2356

[53] Luo J W, Stradins P and Zunger A 2011 *Energy Environ. Sci.* **4** 2546

[54] Wang L W and Zunger A 1994 *J. Chem. Phys.* **100** 2394

[55] Chuang S L 2009 *Physics of Photonic Devices* (Hoboken: Wiley)

[56] Yu P Y and Cardona M 2005 *Fundamentals of Semiconductors: Physics and Materials Properties*, 3rd edn. (Berlin: Springer)

[57] Li Y, Song Z, Li Z, Sun G, Tan C S, Fan W and Wang Q J 2020 *New J. Phys.* **22** 83061

[58] Koster G F, Dimmock J O, Wheeler R G and Statz H 1963 *The properties of the thirty-two point groups* (Cambridge, MA: MIT Press)

[59] Yeh C Y, Wei S H and Zunger A 1994 *Phys. Rev. B* **50** 2715

[60] Vurgaftman I, Meyer J R and Ram-Mohan L R 2001 *J. Appl. Phys.* **89** 5815

[61] Bechstedt F and Belabbes A 2013 *J. Phys.: Condens. Matter* **25** 273201

[62] Fadaly E M T, Marzegalli A, Ren Y, Sun L, Dijkstra A, De Matteis D, Scalise E, Sarikov A, De Luca M, Rurali R, Zardo I, Haverkort J E M, Botti S, Miglio L, Bakkers E P A M and Verheijen M A 2021 *Nano Lett.* **21** 3619

[63] Berghuis W J H W J, Van Tilburg M A J, Peeters W H J, Van Lange V T, Farina R, Fadaly E M T, Renirie E C M, Theeuwes R J, Verheijen Marcel A, Macco B, Bakkers E P A M, Haverkort J E M and Kessels W M M E 2024 *ACS Appl. Nano Mater.* **7** 2343

[64] Li Z H, Wang M L, Kong Z Z, Wang G L, Kang Y, Xu Y Q, Wu R, Hao T Y, Wei Z C, Wang B C, Li H O, Cao G and Guo G P 2025 *Chin. Phys. B* **34** 90305

[65] Amato M, Kaewmaraya T, Zobelli A, Palummo M and Rurali R 2016 *Nano Lett.* **16** 5694

[66] Kim J M, Haque M F, Hsieh E Y, Nahid S M, Zarin I, Jeong K Y, So J P, Park H G and Nam S 2023 *Adv. Mater.* **35** 2107362

[67] Dai Z, Liu L and Zhang Z 2019 *Adv. Mater.* **31** 1805417

[68] Carroll L, Friedli P, Neuenschwander S, Sigg H, Cecchi S, Isa F, Chrastina D, Isella G, Fedoryshyn Y and Faist J 2012 *Phys. Rev. Lett.* **109** 57402

[69] Bao S, Kim D, Onwukaeme C, Gupta S, Saraswat K, Lee K H, Kim Y, Min D, Jung Y, Qiu H, Wang H, Fitzgerald E A, Tan C S and Nam D 2017 *Nat. Commun.* **8** 1845

[70] Pilon F A, Niquet Y M, Chretien J, Pauc N, Reboud V, Calvo V, Widiez J, Hartmann J M, Chelnokov A, Faist J and Sigg H 2022 *Phys. Rev. Res.* **4** 33050

[71] Süess M J, Geiger R, Minamisawa R A, Schiefler G, Frigerio J, Chrastina D, Isella G, Spolenak R, Faist J and Sigg H 2013 *Nat. Photonics* **7** 466

[72] Gassenq A, Tardif S, Guilloy K, Osvaldo Dias G, Pauc N, Duchemin I, Rouchon D, Hartmann J M, Widiez J, Escalante J, Niquet Y M, Geiger R, Zabel T, Sigg H, Faist J, Chelnokov A, Rieutord F, Reboud V and Calvo V 2016 *Appl. Phys. Lett.* **108** 241902

[73] Signorello G, Lörtscher E, Khomyakov P A, Karg S, Dheeraj D L, Gotsmann B, Weman H and Riel H 2014 *Nat. Commun.* **5** 3655

[74] Wei B, Zheng K, Ji Y, Zhang Y, Zhang Z and Han X 2012 *Nano Lett.* **12** 4595

[75] Zeng L, Gammer C, Ozdol B, Nordqvist T, Nygård J, Krogstrup P, Minor A M, Jäger W and Olsson E 2018 *Nano Lett.* **18** 4949

[76] Song X, Zhang T, Wu L, Hu R, Qian W, Liu Z, Wang J, Shi Y, Xu J, Chen K and Yu L 2022 *Adv. Sci.* **9** 2105623